

Dynamics of an internally actuated weakly elastic sphere in a general quadratic flow

Shashikant Verma and Navaneeth K. Marath

*Department of Mechanical Engineering,
Indian Institute of Technology, Ropar 140001, India*

(Dated: December 10, 2025)

Abstract

Internally actuated elastic particles are widely used in biomedical applications. It is imperative to understand the dynamics of such particles in pressure-driven microfluidic devices to manipulate their motion. We analytically examine the dynamics of an internally actuated elastic particle translating in a general unbounded quadratic flow in the inertialess limit. We consider the particle as a compressible weakly elastic sphere, and its motion is controlled by applying an external point force and a point torque at the centre of its undeformed shape. The fluid and the particle are modelled using the Stokes and the Navier elasticity equations, respectively. We use the domain perturbation method to capture the particle deformation. The point force and the point torque are obtained until $O(\alpha^2)$, assuming $\alpha \ll 1$. Here, α is the measure of the particle elastic strain induced due to the fluid viscous stress. We present the results for the particle motion in a general unbounded quadratic flow. The results are simplified further for the motion along the centreline in the quadratic component of three Poiseuille flows: 1) elliptical Poiseuille, 2) plane Poiseuille, and 3) Hagen-Poiseuille flows. In the general quadratic flow, the point force at $O(\alpha)$ is aligned with the particle velocity, while the force at $O(\alpha^2)$ acts at an angle to the velocity. Furthermore, the torque is non-zero due to elastic effects at $O(\alpha)$ and $O(\alpha^2)$. For all the three Poiseuille flows, the point force until $O(\alpha^2)$ is aligned with the particle velocity, while the torque comes as zero.

I. INTRODUCTION

Internally actuated elastic particles are used in many biomedical applications. A notable example of such particles is magneto-responsive polymer beads[1] consisting of a polymer matrix embedded with magnetic nano- or microparticles (MPs). The polymer provides structural integrity and elasticity, while the embedded MPs impart magnetic responsiveness. These polymer beads are widely used in *in vitro* magnetic separation of biological cells[1, 2] and in targeted drug delivery.[3] By binding to non-magnetic particles, magnetically responsive beads enable their controlled manipulation under externally applied magnetic fields.[1, 4, 5] The MPs are distributed either uniformly or non-uniformly within the polymer matrix.[1] Fig. 1(a) presents a schematic of MPs embedded within a polymer bead. Each embedded magnetic particle responds to the external magnetic field as a localised force that internally actuates the particle. Additionally, MPs can also experience localised torques when subjected to a rotating magnetic field.[6] The localised forces and torques can be modelled as point forces and point torques, respectively. Such a model has been employed to analytically investigate the dynamics of a weakly elastic sphere (embedded with a single magnetic particle at its centre) translating parallel to a rigid wall.[7] The dynamics and deformed shape of a particle moving in a microchannel are determined by the force distribution acting on the particle. For instance, a body force distributed throughout the particle volume yields different dynamics than a localised body force. To analyse the dynamics of internally actuated particles in pressure-driven microfluidic devices, it is imperative to understand their behaviour in quadratic flows. Pressure-driven flows such as Poiseuille flows in elliptical channels, cylindrical tubes and between parallel plates are composed of uniform, linear and quadratic components. In particular, along the centreline of channels/tubes, the linear component vanishes and the particle that is translating with the local ambient velocity experiences only a quadratic component of the flow. Understanding the particle motion along the centreline is important in flow cytometry.[8, 9]

Several studies have analysed the dynamics of rigid[10, 11] and deformable particles[12, 13] in quadratic flows. Theoretical analysis has been carried out to understand the motion and deformation of a spherical drop in quadratic flows, such as paraboloidal and stagnation flows,[12] and in nonlinear cubic shear flows.[14] Yang and Lee[12] have derived the generalised form of Faxen's law for a spherical drop immersed in an arbitrary Stokes flow. The nonlinearity of the cubic shear flow deforms the drop [viscosity ratio of $O(1)$] and sometimes aligns it into two different orientations, at $\pm 45^\circ$ to the flow. A deformable spherical drop in an unbounded Poiseuille

flow exhibits lateral migration toward the channel centreline, depending on the product of the Hadamard-Rybczynski terminal settling velocity and the maximum Poiseuille flow velocity.[15] Stokes flow around a nearly spherical drop in a general quadratic flow has been determined using the vectorial form of Lamb's general solution to the Stokes equations.[13] Recently, the hydrodynamics and morphology of a spherical active compound drop have been analysed in the general quadratic flow.[16] The results from these studies[13, 16] have shown that an initially spherical simple or compound drop deforms into a three-lobe shape under the influence of the hexapolar component of the quadratic flow. Experimentally, it has been observed that the initial spherical simple drop deforms to approximately the three-lobe shape when it is subjected to the hexapolar quadratic flow.[17]

While the dynamics of drops in the quadratic flow has been extensively studied, that of elastic particles remains less explored. The key difference between the behaviour of a drop and an elastic particle comes from the distinct constitutive and governing equations that describe their motion and deformation. Elastic particles as cell models are studied for their potential in diagnosing diseases through mechanical-property-dependent flow behaviour.[18, 19] Further, predicting the internal stresses is important in cells such as white blood cells and osteoblasts, as the stresses can alter the expression of certain genes and, consequently, alter cellular properties.[20–22] Modelling these cells as elastic particles helps in such predictions. Particle elasticity also plays a crucial role in drug delivery processes, as stiffer hydrogel particles are often internalised by immune cells more effectively than softer ones.[23] One of the earlier works in modelling a particle as an elastic solid was carried out by Tam,[24] who studied the dynamics of a compressible elastic sphere in an unbounded simple shear flow. Murata has captured the dynamics of a compressible elastic sphere, sedimenting in an unbounded quiescent fluid[25] and also studied the dynamics of an incompressible elastic sphere in an arbitrary flow field,[26] in the Stokes limit. Finney et al.[22] have examined the influence of channel confinement on the deformation of an incompressible elastic sphere, subjected to an axial body force and translating along the centreline of a rigid cylindrical tube using analytical and numerical techniques. They find that the deformed shape of the sphere can be bullet-like, an anti-bullet or spherical, depending on the strength of the applied body force relative to the viscous force.

In the present work, we analyse the dynamics of an internally actuated weakly elastic spherical particle translating in a general unbounded quadratic flow. We assume that the particle is a homogeneous, isotropic, compressible Hookean solid and contains a centrally embedded magnetic

particle. The motion of the particle is controlled by a localised force/torque, modelled as a point force/torque, induced by an external magnetic field. We use the domain perturbation method and series solutions to the governing equations of the particle and the fluid. First, we present the results for the particle translating in general quadratic flow and then the results are simplified for particle translating along the centreline in the quadratic component of three fully developed flows: 1) flow through the straight rigid tube of the elliptic cross section with a and b being the semi-minor and semi-major axes, respectively, called elliptical Poiseuille flow shown in Fig. 1(b), 2) flow between two infinite parallel rigid plates separated by a distance $2h$ apart, called plane Poiseuille flow shown in Fig. 1(c), and 3) flow inside a straight rigid cylindrical tube of radius R_t , called Hagen-Poiseuille flow shown in Fig. 1(d).

We observe that, in general quadratic flow, the point force arising from elastic effects appears at $O(\alpha)$ and is aligned with the particle velocity, whereas the force at $O(\alpha^2)$ acts at an angle to it. However, in all three Poiseuille flows we considered, the force until $O(\alpha^2)$ remains aligned with the particle velocity. The point torque is nonzero at both $O(\alpha)$ and $O(\alpha^2)$ in general quadratic flow but vanishes when the particle translates along the centreline in Poiseuille flows. The leading-order deformed shape of the particle is compared with that of a spherical active compound drop (active particle embedded inside the drop)[16] in plane Poiseuille flow. The compressible nature of the elastic particle leads to certain morphological differences between the elastic particle and the drop.

The paper is structured as follows. In Section II, we present the governing equations for both the fluid and the particle, along with the quadratic component of a general ambient flow. We also discuss series solutions to the Stokes and Navier elasticity equations, as well as the domain perturbation method. In Section III, we present the results for the general quadratic flow and for the quadratic components of the elliptical Poiseuille, plane Poiseuille and Hagen-Poiseuille flows. We plot the streamlines near the particle and its deformed shape. The leading-order deformed shape of the particle in a plane Poiseuille flow is compared with a drop. Finally, we present the summary of the main results and key observations in Section IV.

II. MATHEMATICAL FORMULATION

We consider a weakly elastic spherical particle of undeformed radius (R_0) moving in a general unbounded quadratic flow. An external point force and a point torque are applied at the centre of the undeformed particle to translate it at a velocity $V_0\hat{\mathbf{k}}$, as shown in Fig. 1(a). We assume

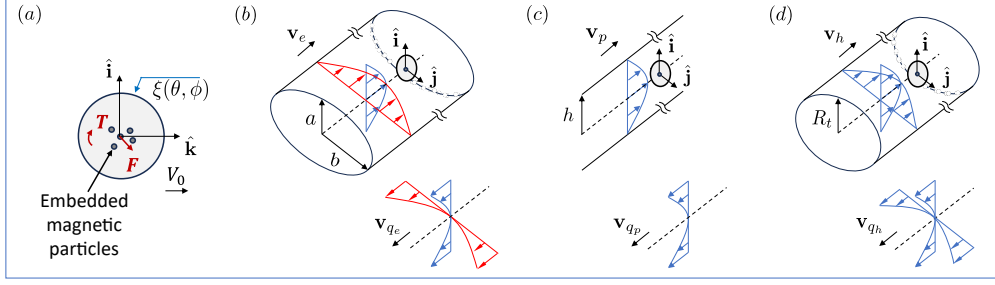


FIG. 1. (a) Schematic of Fe_3O_4 nanoparticles embedded in a polymer bead.[27] Schematic of an elastic sphere translating with velocity $V_0 \hat{\mathbf{k}}$ along the centerline of a channel: (b) inside a straight tube of elliptic cross-section, with a and b as the semi-minor and semi-major axes, respectively; elliptic Poiseuille flow (\mathbf{v}_e , top subfigure) and its quadratic component (\mathbf{v}_{q_e} , bottom subfigure), (c) between two infinite parallel plates separated by a distance $2h$; plane Poiseuille flow (\mathbf{v}_p , top subfigure) and its quadratic component (\mathbf{v}_{q_p} , bottom subfigure), and (d) inside a cylindrical tube of radius R_t ; Hagen-Poiseuille flow (\mathbf{v}_h , top subfigure) and its quadratic component (\mathbf{v}_{q_h} , bottom subfigure). The sphere is subjected to an external point force (\mathbf{F}) and a point torque (\mathbf{T}).

that the viscous effects dominate over the inertial effects, i.e the Reynolds number, defined as $Re = \rho_f V_0 R_0 / \mu \ll 1$. Here, μ and ρ_f are the fluid viscosity and density, respectively. The fluid is considered Newtonian and incompressible, and is governed by the Stokes equations given by

$$-\nabla p + \mu \nabla^2 \mathbf{v} = 0, \quad (1)$$

$$\nabla \cdot \mathbf{v} = 0. \quad (2)$$

In eqn (1) and (2), p and \mathbf{v} are the pressure and velocity fields in the fluid, respectively. The particle is modelled using the Navier elasticity equations given by

$$[\lambda + G] \nabla (\nabla \cdot \mathbf{u}) + G \nabla^2 \mathbf{u} + \mathbf{F} \delta(\mathbf{x}) + \frac{1}{2} [\nabla \delta(\mathbf{x}) \times \mathbf{T}] = 0. \quad (3)$$

Here, λ and G are the Lamé's constants and \mathbf{u} is the displacement field in the particle. The fluid stress ($\boldsymbol{\sigma}$) is given by

$$\boldsymbol{\sigma} = -p \mathbf{I} + \mu (\nabla \mathbf{v} + [\nabla \mathbf{v}]^T) \quad (4)$$

and the solid stress ($\hat{\boldsymbol{\sigma}}$) is given by

$$\hat{\boldsymbol{\sigma}} = \lambda (\nabla \cdot \mathbf{u}) \mathbf{I} + G (\nabla \mathbf{u} + [\nabla \mathbf{u}]^T). \quad (5)$$

The variables in the present analysis are non-dimensionalised using the following scalings

$$\mathbf{v}^* = \frac{\mathbf{v}}{V_0}; p^* = \frac{pR_0}{\mu V_0}; \boldsymbol{\sigma}^* = \frac{\boldsymbol{\sigma}R_0}{\mu V_0}; \mathbf{u}^* = \frac{\mathbf{u}}{R_0}; \hat{\boldsymbol{\sigma}}^* = \frac{\hat{\boldsymbol{\sigma}}}{G}. \quad (6)$$

The ratio of the particle bulk modulus (λ) to its shear modulus (G) is represented by Γ ; $\Gamma = \lambda/G$. Deformability of the particle can be expressed as a measure of elastic strain induced in the particle due to fluid viscous stress, given by $\alpha = \mu V_0/(GR_0)$. [7, 22] The parameter α can also be defined as an elastic capillary number, quantifying the ratio of viscous to elastic stress, [19] or as the ratio of viscous to elastic force. [25, 26, 28] The non-dimensional variables in eqn (6) are denoted using an asterisk symbol, and the symbol is omitted hereafter for convenience.

To analyse the particle dynamics, we solve eqn (1)-(3) in a spherical coordinate system (r, θ, ϕ), whose origin coincides with the centre of the undeformed particle. The solutions are expressed in terms of the non-dimensional radial coordinate ($\xi = r/R_0$), the polar (θ) and the azimuthal (ϕ) angles. The particle is assumed to deform to a steady shape with surface radius given by

$$\xi = 1 + f(\theta, \phi). \quad (7)$$

Here, f quantifies the surface deformation and depends on both the polar and azimuthal angles. The displacement of a material point on the deformed surface, relative to its position on the undeformed surface, is expressed in terms of f as

$$1 = [1 + f - u_r|_{\xi=1+f(\theta,\phi)}]^2 + [u_\theta|_{\xi=1+f(\theta,\phi)}]^2 + [u_\phi|_{\xi=1+f(\theta,\phi)}]^2. \quad (8)$$

Eqn (8) indicates that, for any material point on the deformed surface, the magnitude of the difference between its current position and the displacement it experienced is equal to one. In the weakly deformable limit ($\alpha \ll 1$), the shape of the particle deviates slightly from that of a sphere. We expand all the variables in the problem in the form of regular asymptotic expansions and use the domain perturbation method. [29, 30] The corresponding modified boundary conditions are obtained at different orders in α . The series solutions to the Stokes and elasticity equations are used to obtain the variables that satisfy the modified boundary conditions. In the following discussion, we represent the quantities using either boldface or index notation, choosing whichever form is simpler for a given expression.

In general, the ambient velocity field at an arbitrary point relative to the particle centre [$\mathbf{v}^\infty(\mathbf{x})$] is obtained by expanding the field about the centre of the particle using a Taylor series as given by

$$\mathbf{v}^\infty(\mathbf{x}) = \mathbf{v}^\infty(\mathbf{x} = 0) + \mathbf{x} \cdot \nabla \mathbf{v}^\infty(\mathbf{x} = 0) + \frac{1}{2} [\mathbf{xx} : \nabla \nabla \mathbf{v}^\infty(\mathbf{x} = 0)] + \dots \quad (9)$$

The first, second, and third terms on the right-hand side of eqn (9) are the uniform, linear, and quadratic components of the ambient flow, respectively. In the present work, we consider the quadratic component as the ambient flow (\mathbf{v}_q) for the particle. We refer to the unbounded ambient flow (\mathbf{v}_q) as the general quadratic flow. The flow can be expressed in terms of a third-rank tensor K_{ijk} [13] and is given by

$$(v_q)_k = x_i x_j K_{ijk}, \quad (10)$$

$$K_{ijk} = \frac{1}{2} \nabla_i \nabla_j v_k^\infty(\mathbf{x} = 0). \quad (11)$$

In eqn (10) and (11), K_{ijk} is symmetric with respect to the first two indices. Further, K_{ijk} can be expressed in terms of irreducible components that are first-, second-, and third-order tensors represented by τ , \mathbf{Q} and γ , respectively.[13, 31] The tensors are given by

$$\tau_l = K_{ppl}, \quad (12)$$

$$Q_{lm} = K_{lpq} \epsilon_{qpm} + K_{mpq} \epsilon_{qpl} \text{ and} \quad (13)$$

$$\gamma_{ijk} = \frac{1}{3} (K_{ijk} + K_{kij} + K_{jki}) - \frac{1}{15} (\delta_{ij} K_{ppk} + \delta_{ik} K_{ppj} + \delta_{jk} K_{ppi}). \quad (14)$$

The components \mathbf{Q} and γ are symmetric and traceless with respect to any pair of their indices. The velocity and pressure fields of the general quadratic flow can be expressed in terms of the irreducible components as

$$(v_q)_k = x_i x_j \gamma_{ijk} - \frac{1}{3} (\epsilon_{kij} x_l Q_{lij}) + \frac{1}{5} (2\xi^2 \delta_{kj} - x_k x_j) \tau_j \quad (15)$$

and

$$p_q = P_0 + 2(\tau_i x_i), \quad (16)$$

respectively. Here, P_0 is the reference pressure at the centre of the undeformed particle. In our analysis, we assume the flow component τ and the velocity of the particle are both aligned with the z -axis. The assumption is justified by the fact that the τ , corresponding to the quadratic component of the Poiseuille flow, is aligned with the channel length (z -axis). In addition, the general quadratic flow exerts a hydrodynamic force at the leading-order along τ and the particle is constrained to move with a fixed velocity in the same direction. Hence, both τ and the particle velocity are taken along the z -axis. We discuss the series solutions to the governing equations in Section II A and the domain perturbation method in Section II B. We provide the solution procedure to obtain the variables (\mathbf{v} , σ , p , \mathbf{u} , f , $\hat{\sigma}$, \mathbf{F} , \mathbf{T}) in Section II C.

A. Series solutions to the Stokes and Navier elasticity equations

The series solutions in the spherical coordinate system to eqn (1) and (2) are given in Appendix A, while the solution to eqn (3) is given in Appendix B. In the solution given in eqn (B1)-(B3), the point force and the point torque are denoted by F_i and T_i (with $i = x, y, z$ being the Cartesian components), respectively. The displacement field corresponding to the point force and the point torque decays as $1/\xi$ and $1/\xi^2$, respectively [for details, see Appendix A of Verma et al.[7]]. We analyse the problem in a particle-fixed coordinate system whose origin coincides with the centre of the undeformed particle, and the point torque inhibits the rotation of the particle. The constants that correspond to pure translation ($c1[0, 1]$, $c1[1, 1]$, and $c0[1, 1]$) and pure rotation with no deformation ($a1[0, 1]$, $a1[1, 1]$, and $a0[1, 1]$) in the series solution given in eqn (B1)-(B3) are, therefore, set to zero.

B. Domain perturbation method

In this section, we discuss the domain perturbation method, following the approach outlined in Verma et al.[7] The method is used to transfer the boundary conditions from the deformed surface of the particle to its undeformed surface.[29, 30] The surface deformation f defined in eqn (7) must be determined as a part of the solution. The velocity boundary condition (no-slip and no-penetration) on the deformed surface is given by

$$\mathbf{v} = 0, \quad (17)$$

where $\mathbf{v} = \mathbf{v}_d + \mathbf{v}_q - 1\hat{\mathbf{k}}$. The disturbance velocity and the general quadratic flow fields are denoted by \mathbf{v}_d and \mathbf{v}_q , respectively. The stress continuity on the deformed surface is given by

$$\hat{\boldsymbol{\sigma}} \cdot \hat{\mathbf{n}} = \alpha \boldsymbol{\sigma} \cdot \hat{\mathbf{n}}. \quad (18)$$

Here, $\hat{\mathbf{n}}$ is the outward unit normal from the deformed surface, defined by $\hat{\mathbf{n}} = (\nabla S / |\nabla S|)$, where $S = \xi - 1 - f(\theta, \phi)$. The stress boundary conditions in terms of different stress components are given by

$$\hat{\boldsymbol{\sigma}}_{rr} - \frac{\hat{\boldsymbol{\sigma}}_{r\theta}}{\xi} \frac{\partial f}{\partial \theta} - \frac{\hat{\boldsymbol{\sigma}}_{r\phi}}{\xi \sin \theta} \frac{\partial f}{\partial \phi} = \alpha \left[\boldsymbol{\sigma}_{rr} - \frac{\boldsymbol{\sigma}_{r\theta}}{\xi} \frac{\partial f}{\partial \theta} - \frac{\boldsymbol{\sigma}_{r\phi}}{\xi \sin \theta} \frac{\partial f}{\partial \phi} \right], \quad (19)$$

$$\hat{\boldsymbol{\sigma}}_{r\theta} - \frac{\hat{\boldsymbol{\sigma}}_{\theta\theta}}{\xi} \frac{\partial f}{\partial \theta} - \frac{\hat{\boldsymbol{\sigma}}_{\theta\phi}}{\xi \sin \theta} \frac{\partial f}{\partial \phi} = \alpha \left[\boldsymbol{\sigma}_{r\theta} - \frac{\boldsymbol{\sigma}_{\theta\theta}}{\xi} \frac{\partial f}{\partial \theta} - \frac{\boldsymbol{\sigma}_{\theta\phi}}{\xi \sin \theta} \frac{\partial f}{\partial \phi} \right] \quad (20)$$

and

$$\hat{\sigma}_{r\phi} - \frac{\hat{\sigma}_{\theta\phi}}{\xi} \frac{\partial f}{\partial \theta} - \frac{\hat{\sigma}_{\phi\phi}}{\xi \sin \theta} \frac{\partial f}{\partial \phi} = \alpha \left[\sigma_{r\phi} - \frac{\sigma_{\theta\phi}}{\xi} \frac{\partial f}{\partial \theta} - \frac{\sigma_{\phi\phi}}{\xi \sin \theta} \frac{\partial f}{\partial \phi} \right]. \quad (21)$$

Here, the $\hat{\sigma}_{ij}$ and σ_{ij} with $i, j = r, \theta, \phi$ are the components of the solid and fluid stress tensors, respectively. In the domain perturbation method, we first performed a Taylor series expansion of the boundary conditions, defined in eqn (17)-(21) about $\xi = 1$, and then the regular asymptotic expansions of the variables in the problem are substituted into these expanded boundary conditions. The regular expansions of the variables as series in α are given by

$$\mathbf{v} = \mathbf{v}^{(0)} + \alpha \mathbf{v}^{(1)} + \alpha^2 \mathbf{v}^{(2)} + \dots, \quad (22)$$

$$\boldsymbol{\sigma} = \boldsymbol{\sigma}^{(0)} + \alpha \boldsymbol{\sigma}^{(1)} + \alpha^2 \boldsymbol{\sigma}^{(2)} + \dots, \quad (23)$$

$$p = p^{(0)} + \alpha p^{(1)} + \alpha^2 p^{(2)} + \dots, \quad (24)$$

$$\mathbf{u} = \alpha \mathbf{u}^{(1)} + \alpha^2 \mathbf{u}^{(2)} + \dots, \quad (25)$$

$$f = \alpha f^{(1)} + \alpha^2 f^{(2)} + \dots, \quad (26)$$

$$\hat{\boldsymbol{\sigma}} = \alpha \hat{\boldsymbol{\sigma}}^{(1)} + \alpha^2 \hat{\boldsymbol{\sigma}}^{(2)} + \dots, \quad (27)$$

$$\mathbf{F} = \mathbf{F}^{(0)} + \alpha \mathbf{F}^{(1)} + \alpha^2 \mathbf{F}^{(2)} + \dots \quad (28)$$

and

$$\mathbf{T} = \mathbf{T}^{(0)} + \alpha \mathbf{T}^{(1)} + \alpha^2 \mathbf{T}^{(2)} + \dots \quad (29)$$

It is important to note that the leading-order terms in the series of the displacement field [eqn (25)], surface deformation [eqn (26)], and solid stress field [eqn (27)] arising from the deformation appear at $O(\alpha)$.

1. Modified velocity boundary conditions on the undeformed surface ($\xi = 1$)

The Taylor series expansion of eqn (17) about the undeformed surface ($\xi = 1$) is carried out, and the expansion of velocity and surface deformation from eqn (22) and (26), respectively, are substituted to obtain the modified velocity boundary conditions at successive orders in α . At leading-order, the boundary conditions are given by

$$\mathbf{v}^{(0)} = 0 \text{ as } \xi = 1, \quad (30)$$

$$\rightarrow \mathbf{v}_q - 1 \hat{\mathbf{k}} \text{ as } \xi \rightarrow \infty. \quad (31)$$

At $O(\alpha)$, it is

$$\mathbf{v}^{(1)} + f^{(1)} \frac{\partial \mathbf{v}^{(0)}}{\partial \xi} = 0 \quad (32)$$

and at $O(\alpha^2)$, it is

$$\mathbf{v}^{(2)} + f^{(1)} \frac{\partial \mathbf{v}^{(1)}}{\partial \xi} + f^{(2)} \frac{\partial \mathbf{v}^{(0)}}{\partial \xi} + \frac{[f^{(1)}]^2}{2} \frac{\partial^2 \mathbf{v}^{(0)}}{\partial \xi^2} = 0. \quad (33)$$

The velocity fields $\mathbf{v}^{(1)}$ and $\mathbf{v}^{(2)}$ are the disturbance fields and decay as $\xi \rightarrow \infty$. Note that the boundary conditions in eqn (32) and (33) are nonlinear. Although the governing equations are linear, the nonlinearity stems from the fact that the unmodified boundary conditions are applied on the deformed surface, whose shape is a part of the solution.

2. Modified stress boundary conditions on the undeformed surface ($\xi = 1$)

The Taylor series expansion of eqn (18) about the undeformed surface ($\xi = 1$) is carried out, and the expansions of fluid stress, surface deformation, and solid stress from eqn (23), (26), and (27), respectively, are substituted to obtain the modified stress boundary conditions at various orders in α . At $O(\alpha)$, the stress boundary conditions are

$$\hat{\sigma}_{rr}^{(1)} = \sigma_{rr}^{(0)}, \quad (34)$$

$$\hat{\sigma}_{r\theta}^{(1)} = \sigma_{r\theta}^{(0)}, \quad (35)$$

$$\hat{\sigma}_{r\phi}^{(1)} = \sigma_{r\phi}^{(0)} \quad (36)$$

and at $O(\alpha^2)$, they are

$$\hat{\sigma}_{rr}^{(2)} = \sigma_{rr}^{(1)} + f^{(1)} \frac{\partial}{\partial \xi} [\sigma_{rr}^{(0)} - \hat{\sigma}_{rr}^{(1)}], \quad (37)$$

$$\begin{aligned} \hat{\sigma}_{r\theta}^{(2)} = & \sigma_{r\theta}^{(1)} - f^{(1)} \frac{\partial}{\partial \xi} [\hat{\sigma}_{r\theta}^{(1)} - \sigma_{r\theta}^{(0)}] + \frac{\partial f^{(1)}}{\partial \theta} [\hat{\sigma}_{\theta\theta}^{(1)} - \sigma_{\theta\theta}^{(0)}] \\ & + \frac{1}{\sin \theta} \frac{\partial f^{(1)}}{\partial \phi} [\hat{\sigma}_{\theta\phi}^{(1)} - \sigma_{\theta\phi}^{(0)}], \end{aligned} \quad (38)$$

$$\begin{aligned} \hat{\sigma}_{r\phi}^{(2)} = & \sigma_{r\phi}^{(1)} - f^{(1)} \frac{\partial}{\partial \xi} [\hat{\sigma}_{r\phi}^{(1)} - \sigma_{r\phi}^{(0)}] + \frac{\partial f^{(1)}}{\partial \theta} [\hat{\sigma}_{\theta\phi}^{(1)} - \sigma_{\theta\phi}^{(0)}] \\ & + \frac{1}{\sin \theta} \frac{\partial f^{(1)}}{\partial \phi} [\hat{\sigma}_{\phi\phi}^{(1)} - \sigma_{\phi\phi}^{(0)}]. \end{aligned} \quad (39)$$

The surface deformation at different orders in α , such as $f^{(1)}$ and $f^{(2)}$ appearing in the modified boundary conditions are obtained by expanding eqn (8) using the Taylor series about $\xi = 1$, followed by substituting eqn (25) and (26). At $O(\alpha)$, $f^{(1)}$ is given by

$$f^{(1)} = u_r^{(1)} \Big|_{\xi=1} . \quad (40)$$

At $O(\alpha^2)$, $f^{(2)}$ is given by

$$f^{(2)} = \left(u_r^{(2)} + f^{(1)} \frac{\partial u_r^{(1)}}{\partial \xi} - \frac{[u_\theta^{(1)}]^2 + [u_\phi^{(1)}]^2}{2} \right) \Big|_{\xi=1} . \quad (41)$$

The modified boundary conditions derived in this section, along with the series solutions described in the previous sections, are used to calculate all the variables defined in eqn (22)-(29).

C. Solution procedure

Here, we describe the steps involved in calculating the velocity, pressure, displacement, point force, and point torque until $O(\alpha^2)$, as the particle translates in the general quadratic flow.

1. At $O(1)$, the constants in Appendix A, eqn (A1)-(A3) are determined by applying the velocity boundary conditions given in eqn (30) and (31), and corresponding $p^{(0)}$ and $\sigma^{(0)}$ are calculated.
2. Using stress continuity at $O(\alpha)$ given in eqn (34)-(36), the constants in Appendix B that appear in $\hat{\boldsymbol{\sigma}}^{(1)}$, $\mathbf{F}^{(0)}$ and $\mathbf{T}^{(0)}$ are determined. Subsequently, $\mathbf{u}^{(1)}$ and $f^{(1)}$ are calculated.
3. At $O(\alpha)$, the constants in Appendix A, eqns. (A1)(A3), are determined using the velocity boundary condition given in eqn (32) and in turn calculate $p^{(1)}$ and $\sigma^{(1)}$.
4. Using stress continuity at $O(\alpha^2)$ given in eqn (37)-(39), the constants in Appendix B that appear in $\hat{\boldsymbol{\sigma}}^{(2)}$, $\mathbf{F}^{(1)}$ and $\mathbf{T}^{(1)}$ are obtained. Subsequently, $\mathbf{u}^{(2)}$ and $f^{(2)}$ are calculated.

5. At $O(\alpha^2)$, the constants in Appendix A, eqn (A1)-(A3) are determined by applying the velocity boundary condition given in eqn (33) and corresponding $p^{(2)}$ and $\sigma^{(2)}$ are calculated. The point force (torque) at $O(\alpha^2)$ is obtained directly using the fluid stress (moment of fluid stress about origin) at the same order, in the absence of body force as discussed in Appendix C. When the body force (torque) is present, additional terms corresponding to the body force (torque) must be considered. Alternatively, the next-order stress boundary conditions [$O(\alpha^3)$] can be applied to determine the point force and the point torque.

In the next section, we discuss the results of our analysis.

III. RESULTS

First, we analysed the dynamics of the particle and obtained the results in a general quadratic flow. The results are then simplified for the quadratic component of all three Poiseuille flows, as shown in Fig. 1. The confinement ratios in each of the flows are defined based on their geometry. In the elliptical Poiseuille flow, the confinement ratios along the x and y axes are defined as $\psi_x = R_0/a$ and $\psi_y = R_0/b$, respectively. For the plane Poiseuille and Hagen-Poiseuille flows, the confinement ratios are defined as $\psi = R_0/h$ and $\psi = R_0/R_t$, respectively. We considered the confinement ratio to be much less than one, assuming the channel size is much larger than the particle size. We first discuss the expressions of the variables (\mathbf{v} , p , \mathbf{u} , f , \mathbf{F} and \mathbf{T}) and then plot both the streamlines and the deformed shape of the particle in section III D.

Here, we present the results for the particle translating in a general quadratic flow. The components of the disturbance velocity and the pressure fields in the fluid at $O(1)$ and the components of the displacement field at $O(\alpha)$ are given in the ESI[†] (section 1). At $O(\alpha)$, the surface deformation

is obtained as

$$\begin{aligned}
f_q^{(1)} = & \frac{1}{256(2+\Gamma)(2+3\Gamma)} \left[6 \cos \theta (\Gamma^2(128 + 105\gamma_{333}) + 4(80 + 35\gamma_{333} \right. \\
& - 48\tau) + 8\Gamma(64 + 35\gamma_{333} - 16\tau) - 140(2+\Gamma)(2+3\Gamma)(2\gamma_{223} \\
& + \gamma_{333}) \cos 2\phi \sin^2 \theta + (2+\Gamma)(350(2+3\Gamma)\gamma_{333} \cos 3\theta + 35(2 \\
& + 3\Gamma)[-4(4\gamma_{122} + \gamma_{133}) \cos 3\phi \sin^3 \theta + 3\gamma_{233}(\sin \theta + 5 \sin 3\theta) \\
& \times \sin \phi + 3 \cos \phi (\gamma_{133} \sin \theta + 5\gamma_{133} \sin 3\theta + 32\gamma_{123} \cos \theta \sin^2 \theta \\
& \times \sin \phi) - 4(4\gamma_{222} + 3\gamma_{233}) \sin^3 \theta \sin 3\phi] \left. \right] - \frac{P_0}{2+3\Gamma}. \quad (42)
\end{aligned}$$

Here, $\Gamma = \lambda/G$ as defined following eqn (6). Note that the deformation associated with P_0 represents purely radial compression on account of the compressible nature of the particle. The expressions for the components of disturbance velocity ($\mathbf{v}_{d_q}^{(1)}$) and the pressure ($p_{d_q}^{(1)}$) fields at $O(\alpha)$, and the components of displacement ($\mathbf{u}_q^{(2)}$), velocity ($\mathbf{v}_{d_q}^{(2)}$), and the pressure ($p_{d_q}^{(2)}$) fields at $O(\alpha^2)$ are lengthy and omitted here for brevity. The components of $\mathbf{v}_{d_q}^{(1)}$ and the $p_{d_q}^{(1)}$ are obtained by substituting the corresponding constants ($a[m, n]$, $\tilde{a}[m, n]$, $b[m, n]$, $\tilde{b}[m, n]$, $v[m, n]$, and $\tilde{v}[m, n]$) (ESI ‡) in the velocity [eqn (A1)-(A3)] and pressure series [eqn (A4)], respectively. The components of $\mathbf{u}_q^{(2)}$ are obtained by substituting the corresponding constants ($a1[m, n]$, $a0[m, n]$, $b1[m, n]$, $b0[m, n]$, $c1[m, n]$, and $c0[m, n]$) (ESI ‡), in the displacement series [eqn (B1)-(B3)]. Further, the surface deformation at $O(\alpha^2)$ is obtained using eqn (41). At $O(\alpha^2)$, the components of the $\mathbf{v}_{d_q}^{(2)}$ and the $p_{d_q}^{(2)}$ are obtained by substituting the corresponding constants ($a[m, n]$, $\tilde{a}[m, n]$, $b[m, n]$, $\tilde{b}[m, n]$, $v[m, n]$, and $\tilde{v}[m, n]$) (ESI ‡), in the velocity series [eqn (A1)-(A3)] and pressure series [eqn (A4)], respectively. The point force until $O(\alpha^2)$ in dimensional form is obtained as

$$\begin{aligned}
\mathbf{F}_q = & 6\pi\mu V_0 R_0 \left(\left[1 - \frac{\tau}{3} \right] \hat{\mathbf{k}} + \alpha \left[\frac{P_0(\tau-1)}{2+3\Gamma} \right] \hat{\mathbf{k}} + \alpha^2 \frac{2}{3} \left[a[1, 1] \hat{\mathbf{i}} \right. \right. \\
& \left. \left. + \tilde{a}[1, 1] \hat{\mathbf{j}} + a[0, 1] \hat{\mathbf{k}} \right] \right). \quad (43)
\end{aligned}$$

The constants $a[1, 1]$, $\tilde{a}[1, 1]$, and $a[0, 1]$ (ESI ‡) are among the constants determined from the velocity boundary conditions at $O(\alpha^2)$. The leading-order point force in eqn (43) reduces to the Stokes drag on a rigid sphere translating along the τ (z -axis) in the general quadratic flow. Due to the elastic effects, the point force at $O(\alpha)$ acts along the z -axis and is proportional to the reference pressure at the centre of the undeformed sphere [defined following eqn (16)]. It is important to note that the force at $O(\alpha^2)$ has components along all three axes in the general quadratic flow.

However, as we see in later sections, the force acts only along the z -axis in the elliptical Poiseuille, plane Poiseuille, and Hagen-Poiseuille flows. The drag force at the leading-order scales as $\mu V_0 R_0$, at $O(\alpha)$ as $\mu^2 V_0^2 / G$, and at $O(\alpha^2)$ as $(\mu^3 V_0^3 / G^2)(1/R_0)$. The point torque until $O(\alpha^2)$ in dimensional form is obtained as

$$\begin{aligned} \mathbf{T}_q = & 8\pi\mu V_0 R_0^2 \left(\alpha \left[Z_1 \hat{\mathbf{i}} + Z_2 \hat{\mathbf{j}} + Z_3 \hat{\mathbf{k}} \right] + \alpha^2 \left[v[1, 1] \hat{\mathbf{i}} + \tilde{v}[1, 1] \hat{\mathbf{j}} \right. \right. \\ & \left. \left. + v[0, 1] \hat{\mathbf{k}} \right] \right). \end{aligned} \quad (44)$$

The expressions for Z_1 , Z_2 , and Z_3 are given in the ESI[†] (section 1). The constants $v[1, 1]$, $\tilde{v}[1, 1]$, and $v[0, 1]$ (ESI[‡]) are among the constants determined from the velocity boundary conditions at $O(\alpha^2)$. The leading-order point torque in eqn (44) appears at $O(\alpha)$ and exhibits a scaling of $(\mu^2 V_0^2 / G)(R_0)$, while the torque at $O(\alpha^2)$ exhibits a scaling of $(\mu^3 V_0^3 / G^2)$. The components of the torque at $O(\alpha)$ and $O(\alpha^2)$ act along all three axes. However, the torque is found to be zero in all three Poiseuille flows (Fig. 1), consistent with the fact that a particle located at the centreline of the channel does not experience a hydrodynamic torque. We present the simplification of quadratic results in sections III A, III B, and III C. In Poiseuille flows, we constrain the particle to translate with the centreline velocity (V_{max}).

A. Simplification for the elliptical Poiseuille flow

In this section, we present the results for the particle translating along the centreline in the quadratic component of the elliptical Poiseuille flow. The undisturbed velocity field is given by

$$\mathbf{v}_e = \left[1 - \left(\frac{x}{a} \right)^2 - \left(\frac{y}{b} \right)^2 \right] \hat{\mathbf{k}}, \quad (45)$$

The quadratic component of the elliptical Poiseuille flow (\mathbf{v}_{q_e}) is represented in terms of third rank tensor \mathbf{K}_{q_e} as given by

$$\mathbf{v}_{q_e} = \mathbf{xx} : \mathbf{K}_{q_e}, \quad (46)$$

$$\mathbf{K}_{q_e} = - \left[\psi_x^2 \hat{\mathbf{i}} \hat{\mathbf{i}} \hat{\mathbf{k}} + \psi_y^2 \hat{\mathbf{j}} \hat{\mathbf{j}} \hat{\mathbf{k}} \right]. \quad (47)$$

The irreducible components (τ_{q_e} , \mathbf{Q}_{q_e} , and γ_{q_e}) are obtained by substituting eqn (47) in eqn (12)-(14). The corresponding components of the undisturbed velocity and the pressure fields are given

by

$$v_{q_e,r} = -\frac{1}{2} \left[\xi^2 \cos \theta (\psi_x^2 + \psi_y^2 + (\psi_x^2 - \psi_y^2) \cos 2\phi) \sin^2 \theta \right], \quad (48)$$

$$v_{q_e,\theta} = \frac{1}{2} \left[\xi^2 (\psi_x^2 + \psi_y^2 + (\psi_x^2 - \psi_y^2) \cos 2\phi) \sin^3 \theta \right], \quad (49)$$

$$v_{q_e,\phi} = 0 \text{ and} \quad (50)$$

$$p_{q_e} = P_0 - 2\xi (\psi_x^2 + \psi_y^2) \cos \theta, \quad (51)$$

respectively. The ambient field gets disturbed by the translation of the particle. The components of the disturbance velocity ($\mathbf{v}_{d_{qe}}^{(0)}$) and the pressure ($p_{d_{qe}}^{(0)}$) fields in the fluid at the leading-order and the components of the displacement ($\mathbf{u}_{qe}^{(1)}$) field at $O(\alpha)$ are given in the ESI[†] (section 2). The surface deformation at $O(\alpha)$ is obtained as

$$f_{qe}^{(1)} = \frac{1}{8} \left[8(\mathcal{A}_1 + \mathcal{E}_1) - 5\mathcal{A}_3 \cos 2\theta - 5\mathcal{A}_4 \cos 2\phi \sin^2 \theta \right] \cos \theta - \frac{P_0}{2 + 3\Gamma}. \quad (52)$$

The expressions for \mathcal{A}_1 , \mathcal{A}_3 , \mathcal{A}_4 and \mathcal{E}_1 are given in the ESI[†] (section 2). The components of disturbance velocity ($\mathbf{v}_{d_{qe}}^{(1)}$) and the pressure ($p_{d_{qe}}^{(1)}$) fields in the fluid at $O(\alpha)$ and the displacement ($\mathbf{u}_{qe}^{(2)}$) field at $O(\alpha^2)$ are given in the ESI[†] (section 2). At $O(\alpha^2)$, the surface deformation ($f_{qe}^{(2)}$) is obtained as

$$\begin{aligned} f_{qe}^{(2)} = & \mathcal{L}_1 - \mathcal{L}_2 \cos 2\theta + \mathcal{L}_3 \cos 4\theta + \mathcal{L}_4 \cos 6\theta - (\mathcal{L}_5 + \mathcal{L}_6 \cos 2\theta \\ & + \mathcal{L}_7 \cos 4\theta) \cos 2\phi \sin^2 \theta + (\mathcal{L}_8 + \mathcal{L}_9 \cos 2\theta) \cos 4\phi \sin^4 \theta \\ & + P_0^2 [\mathcal{L}_{10}] + P_0 [\mathcal{L}_{11} \cos 3\theta + \cos \theta (\mathcal{L}_{12} + \mathcal{L}_{13} \cos 2\phi \sin^2 \theta)]. \end{aligned} \quad (53)$$

The expressions for \mathcal{L}_n (with $n=1,2,\dots,13$) are given in the ESI[†] (section 2). Note that the surface deformations $f_{qe}^{(1)}$ and $f_{qe}^{(2)}$ are functions of the azimuthal angle (ϕ) due to the asymmetry of the channel geometry about the z -axis. The components of $\mathbf{v}_{d_{qe}}^{(2)}$ and $p_{d_{qe}}^{(2)}$ for the elliptical Poiseuille flow are obtained by substituting the irreducible components γ_{qe} , \mathbf{Q}_{qe} , and $\boldsymbol{\tau}_{qe}$ into the corresponding results ($\mathbf{v}_{d_q}^{(2)}$ and $p_{d_q}^{(2)}$) of the general quadratic flow. The point force until $O(\alpha^2)$ in dimensional

form is obtained as

$$\begin{aligned}
\mathbf{F}_{q_e} = & 6\pi\mu V_0 R_0 \left(\left[1 + \frac{(\psi_x^2 + \psi_y^2)}{3} \right] - \alpha P_0 \left[\frac{1 + \psi_x^2 + \psi_y^2}{(2 + 3\Gamma)} \right] \right. \\
& + \alpha^2 \left[\mathcal{X}_1 + \mathcal{X}_2 \psi_x^2 + \mathcal{X}_3 \psi_x^4 + \mathcal{X}_4 \psi_x^6 + (\mathcal{X}_2 + \mathcal{X}_6 \psi_x^2 \right. \\
& + \mathcal{X}_5 \psi_x^4) \psi_y^2 + (\mathcal{X}_3 + \mathcal{X}_5 \psi_x^2) \psi_y^4 + \mathcal{X}_4 \psi_y^6 \\
& \left. \left. + P_0^2 \left(\frac{1 + 2(\psi_x^2 + \psi_y^2)}{(2 + 3\Gamma)^2} \right) \right] \right) \hat{\mathbf{k}}. \tag{54}
\end{aligned}$$

The expressions for \mathcal{X}_n (with $n = 1, 2, \dots, 6$) are given in the ESI[†] (section 2). The effects of elasticity in eqn (54) appear at $O(\alpha)$ and $O(\alpha^2)$. Additionally, the point force is aligned with the velocity of the particle (z -axis) and balances the hydrodynamic drag. The results of the elliptical Poiseuille flow are further simplified for the plane Poiseuille and Hagen-Poiseuille flows in sections III B and III C, respectively.

B. Simplification for the plane Poiseuille flow

The quadratic flow, along with the disturbance velocity, pressure, displacement, deformation, and point force at different orders in α are obtained for the plane Poiseuille flow by substituting $\psi_x = \psi$ and $\psi_y = 0$ in the corresponding expressions for the elliptical Poiseuille flow. The components of undisturbed velocity and the pressure fields for the quadratic component of the plane Poiseuille flow are obtained as

$$v_{q_p, r} = -\xi^2 \psi^2 \cos \theta \cos^2 \phi \sin^2 \theta, \tag{55}$$

$$v_{q_p, \theta} = \xi^2 \psi^2 \cos^2 \phi \sin^3 \theta, \tag{56}$$

$$v_{q_p, \phi} = 0 \text{ and} \tag{57}$$

$$p_{q_p} = P_0 - 2\xi \psi^2 \cos \theta, \tag{58}$$

respectively. The expressions of \mathcal{A}_n (with $n = 1, 2, 3, 4$), \mathcal{B}_n (with $n = 1$), \mathcal{E}_n (with $n = 1$), \mathcal{F}_n (with $n = 1, 2$), \mathcal{H}_n (with $n = 1, 2, \dots, 22$), \mathcal{I}_n (with $n = 1, 2, \dots, 18$), \mathcal{J}_n (with $n = 1, 2, \dots, 9$), \mathcal{K}_n ($n = 1, 2, \dots, 11$), and \mathcal{L}_n (with $n = 1, 2, \dots, 13$) appearing in field variables for the elliptical Poiseuille flow (section 2, ESI[†]) are simplified to A_n , B_n , E_n , F_n , H_n , I_n , J_n , K_n , and L_n , respectively, and are given in the ESI[†] (section 3).

The surface deformation of the particle until $O(\alpha^2)$ is obtained as

$$f_{q_p} = \alpha f_{q_p}^{(1)} + \alpha^2 f_{q_p}^{(2)} \quad (59)$$

Here,

$$f_{q_p}^{(1)} = \left[A_1 + E_1 - \frac{5}{4} A_3 \left(\frac{\cos 2\theta}{2} - \cos 2\phi \sin^2 \theta \right) \right] \cos \theta - \frac{P_0}{2 + 3\Gamma}, \quad (60)$$

$$\begin{aligned} f_{q_p}^{(2)} = & L_1 - L_2 \cos 2\theta + L_3 \cos 4\theta + L_4 \cos 6\theta - (L_5 + L_6 \cos 2\theta \\ & + L_7 \cos 4\theta) \cos 2\phi \sin^2 \theta + (L_8 + L_9 \cos 2\theta) \cos 4\phi \sin^4 \theta \\ & + P_0^2 L_{10} + P_0 [L_{11} \cos 3\theta + \cos \theta (L_{12} + L_{13} \cos 2\phi \sin^2 \theta)]. \end{aligned} \quad (61)$$

The surface deformation is a function of the azimuthal angle (ϕ) due to the asymmetry of the channel geometry about the z -axis. The point force until $O(\alpha^2)$ in dimensional form is obtained as

$$\begin{aligned} \mathbf{F}_{q_p} = & 6\pi\mu V_0 R_0 \left(\left[1 + \frac{\psi^2}{3} \right] - \alpha P_0 \left[\frac{1 + \psi^2}{(2 + 3\Gamma)} \right] + \alpha^2 \left[\mathcal{X}_1 + \mathcal{X}_2 \psi^2 \right. \right. \\ & \left. \left. + \mathcal{X}_3 \psi^4 + \mathcal{X}_4 \psi^6 + P_0^2 \frac{1 + 2\psi^2}{(2 + 3\Gamma)^2} \right] \right) \hat{\mathbf{k}}. \end{aligned} \quad (62)$$

C. Simplification for the Hagen-Poiseuille flow

Similar to the results obtained for the plane Poiseuille flow, all field quantities at different orders in α are obtained for the Hagen-Poiseuille flow by substituting $\psi_x = \psi_y = \psi$ in the corresponding expressions for the elliptical Poiseuille flow. The components of undisturbed velocity and the pressure fields for the quadratic component of the Hagen-Poiseuille flow are obtained as

$$v_{q_n, r} = -\xi^2 \psi^2 \cos \theta \sin^2 \theta, \quad (63)$$

$$v_{q_n, \theta} = \xi^2 \psi^2 \sin^3 \theta, \quad (64)$$

$$v_{q_n, \phi} = 0 \text{ and} \quad (65)$$

$$p_{q_n} = P_0 - 4\xi \psi^2 \cos \theta, \quad (66)$$

The expressions of \mathcal{A}_n (with $n = 1, 2, 3, 4$), \mathcal{B}_n (with $n = 1$), \mathcal{E}_n (with $n = 1$), \mathcal{F}_n (with $n = 1, 2$), \mathcal{H}_n (with $n = 1, 2, \dots, 22$), \mathcal{I}_n (with $n = 1, 2, \dots, 18$), \mathcal{J}_n (with $n = 1, 2, \dots, 9$), \mathcal{K}_n ($n = 1, 2, \dots, 11$), and \mathcal{L}_n (with $n = 1, 2, \dots, 13$) are simplified to \tilde{A}_n , \tilde{B}_n , \tilde{E}_n , \tilde{F}_n , \tilde{H}_n , \tilde{I}_n , \tilde{J}_n , \tilde{K}_n , and \tilde{L}_n , respectively, and are given in the ESI[†] (section 4).

The surface deformation of the particle until $O(\alpha^2)$ is obtained as

$$f_{qh} = \alpha f_{qh}^{(1)} + \alpha^2 f_{qh}^{(2)} \quad (67)$$

Here,

$$f_{qh}^{(1)} = \left[\tilde{A}_1 + \tilde{E}_1 - \frac{5}{8} \tilde{A}_3 \cos 2\theta \right] \cos \theta - \frac{P_0}{2 + 3\Gamma}, \quad (68)$$

$$f_{qh}^{(2)} = \tilde{L}_1 - \tilde{L}_2 \cos 2\theta + \tilde{L}_3 \cos 4\theta + \tilde{L}_4 \cos 6\theta + P_0^2 \tilde{L}_{10} \\ + P_0 [\tilde{L}_{11} \cos 3\theta + \cos \theta \tilde{L}_{12}]. \quad (69)$$

The expression of surface deformation becomes simpler compared to the elliptical Poiseuille and plane Poiseuille flows, as it no longer depends on the azimuthal angle (ϕ) due to the axisymmetric channel geometry about the z -axis. The point force until $O(\alpha^2)$ in dimensional form is obtained as

$$\mathbf{F}_{qh} = 6\pi\mu V_0 R_0 \left(\left[1 + \frac{2\psi^2}{3} \right] - \alpha P_0 \left[\frac{1 + 2\psi^2}{(2 + 3\Gamma)} \right] + \alpha^2 \left[\mathcal{X}_1 + 2\mathcal{X}_2 \psi^2 \right. \right. \\ \left. \left. + (2\mathcal{X}_3 + \mathcal{X}_6) \psi^4 + 2(\mathcal{X}_4 + \mathcal{X}_5) \psi^6 + P_0^2 \frac{1 + 4\psi^2}{(2 + 3\Gamma)^2} \right] \right) \hat{\mathbf{k}}. \quad (70)$$

D. Analyses of the velocity and deformed shape

In this section, we plot the velocity field and the deformed shape of the particle until $O(\alpha^2)$ for all three Poiseuille flows, as shown in Fig. 1. The representation of streamplots is similar to that used by Chaithanya et al.,[16] who have analysed an active compound drop in a quadratic flow.

1. Velocity field near the elastic particle

We plot the streamlines in the laboratory frame near the particle in one half of the xz -plane for all three Poiseuille flows, since the flow is symmetric about the z -axis in the plane. The confinement ratio is considered the same on the xz -plane in all the three flows. The particle is constrained to move with V_{max} in the quadratic flow, as well as in its irreducible components. The streamlines of the quadratic flow corresponding to the elliptical Poiseuille flow (\mathbf{v}_{qe}) are shown in Fig. 2(a) and those of its irreducible components γ_{qe} , \mathbf{Q}_{qe} and τ_{qe} are shown in Figs. 2(b), (c), and (d), respectively. The streamlines of the total velocity field (ambient plus disturbance field) corresponding to \mathbf{v}_{qe} , and those corresponding to γ_{qe} , \mathbf{Q}_{qe} and τ_{qe} are shown in Figs. 2(e)-(h). The streamlines of the undisturbed velocity field corresponding to γ_{qe} [Fig. 2(b)] exhibit an extensile-compressive

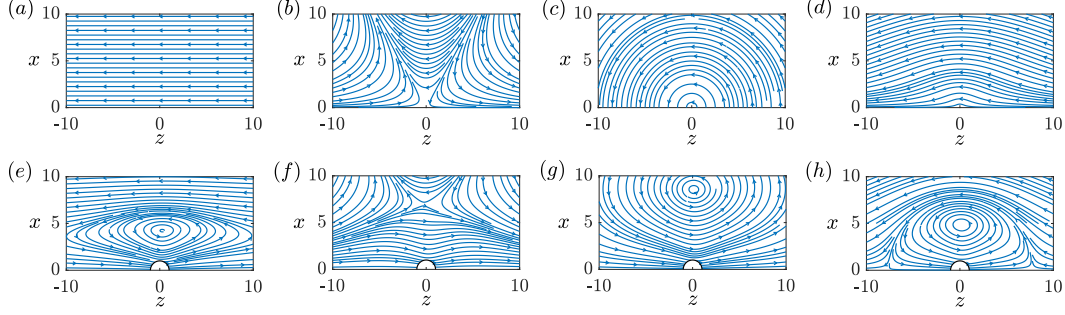


FIG. 2. Streamlines of (a) the quadratic component of elliptical Poiseuille flow and its irreducible components (b) γ_{qe} , (c) \mathbf{Q}_{qe} and (d) τ_{qe} . (e)-(h) are the streamlines of the total velocity field (ambient plus disturbance field) corresponding to (a)-(d), at $\alpha = 0.2$, $\Gamma = 2$, $P_0 = 0.1$, $\psi_x = 0.1$, and $\psi_y = 0.08$.

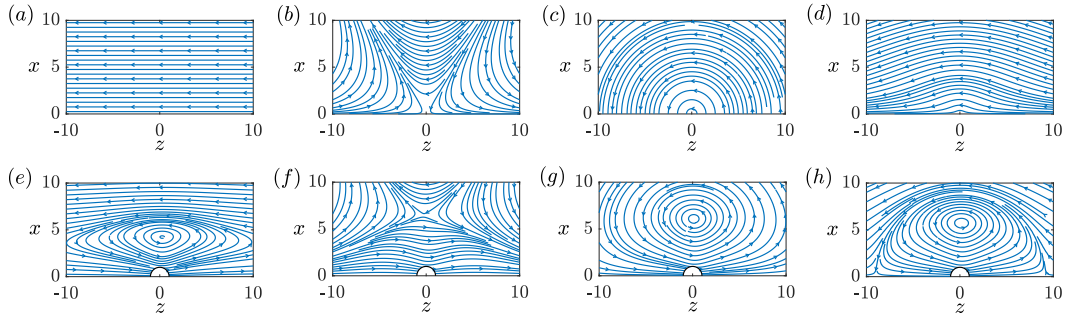


FIG. 3. Streamlines of (a) the quadratic component of plane Poiseuille flow, and its irreducible components (b) γ_{qp} , (c) \mathbf{Q}_{qp} , and (d) τ_{qp} . (e)-(h) are the streamlines of the total velocity field (ambient plus disturbance field) corresponding to (a)-(d), at $\alpha = 0.2$, $\Gamma = 2$, $P_0 = 0.1$, and $\psi = 0.1$.

hexapolar structure. The structure exhibits six distinct principal directions on the xz -plane, with the extensional and compressional states aligned along these principal axes in an alternating manner. The streamlines of the total velocity field (ambient plus disturbance field) associated with γ_{qe} are presented in Fig. 2(f). For \mathbf{Q}_{qe} , the streamlines of the undisturbed velocity field [Fig. 2(c), upper half shown] are circular, featuring opposite axes of rotation in the upper and lower halves of the xz -plane. The streamlines of the corresponding total velocity field are plotted in Fig. 2(g). For τ_{qe} , the streamlines of the undisturbed velocity field [Fig. 2(d)] resembles uniform flow past a rigid sphere, with the associated total velocity field shown in Fig. 2(h). Similarly, we plot the streamlines of the quadratic flow, its irreducible components (top row in the concerned figure), and those of the total velocity field corresponding to the quadratic flow and its irreducible components (bottom row in the concerned figure) for the plane Poiseuille and HagenPoiseuille flows in Figs.

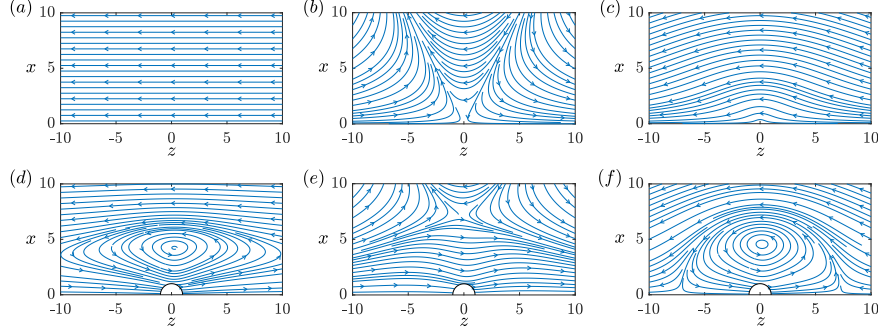


FIG. 4. Streamlines of (a) the quadratic component of Hagen-Poiseuille flow, and its irreducible components (b) γ_{qh} and (c) τ_{qh} . (d)-(f) are the streamlines of the total velocity field (ambient plus disturbance field) corresponding to (a)-(d), at $\alpha = 0.2$, $\Gamma = 2$, $P_0 = 0.1$, and $\psi = 0.1$.

3 and 4, respectively. The streamlines of the total velocity field corresponding to quadratic flow [Figs. 2(e), 3(e), and 4(d)] are almost similar in all three flows. A similar observation also holds for the streamlines corresponding to γ [Figs. 2(f), 3(f), and 4(e)]. The component \mathbf{Q} is zero in the Hagen-Poiseuille flow, while it is non-zero in the elliptical Poiseuille [Fig. 2(c)] and plane Poiseuille [Fig. 3(c)] flows. The centre of the circulation zone in the streamlines of total velocity field, corresponding to \mathbf{Q} , is located away from the particle in the elliptical Poiseuille flow compared to that in the plane Poiseuille flow, as shown in Figs. 2(g) and 3(g), respectively. Further, the location of the centre of the circulation zone in the total velocity field, corresponding to τ , is similar for the elliptical Poiseuille [Fig. 2(h)], plane Poiseuille flow [Fig. 3(h)], and Hagen-Poiseuille [Fig. 4(f)] flows.

2. Deformed shape of the elastic particle

In this section, we discuss the deformed shape of the particle. The shape is plotted in one half of the xz -, yz - and xy -planes for the elliptical Poiseuille [Figs. 5(a)-(c)], plane Poiseuille [Figs. 5(d)-(f)] and Hagen-Poiseuille flows [Figs. 5(g)-(i)], for different confinement ratios. As expected, a larger confinement ratio results in more deformation of the particle compared to that for a lower confinement ratio. In the elliptical Poiseuille and plane Poiseuille flows, the deformed shape is not axisymmetric about the z -axis as seen in Figs. 5(a)-(c) and (d)-(f), respectively. Lack of axisymmetry is due to the asymmetry of the surrounding flow field. The shape is axisymmetric about the z -axis in the Hagen-Poiseuille flow [Figs. 5(g)-(i)]. The dip observed on the left side

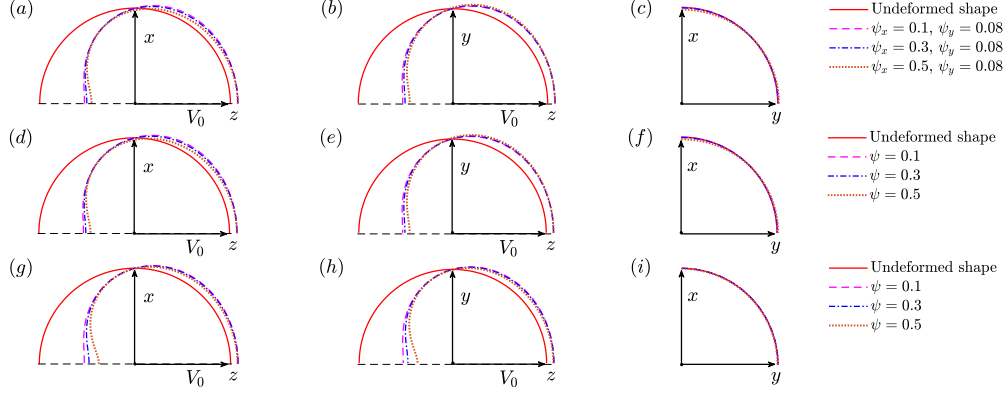


FIG. 5. Deformed shape of the sphere for different confinement ratios, (a)-(c) for elliptical Poiseuille flow, (d)-(f) for plane Poiseuille flow and (g)-(i) for Hagen-Poiseuille flow plotted on the xz -, yz - and xy -planes, respectively, at $\alpha = 0.2$, $P_0 = 0.1$, and $\Gamma = 2$.

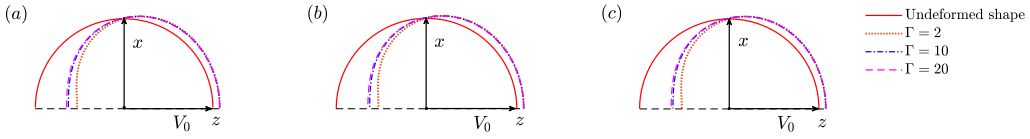


FIG. 6. Deformed shape of the sphere for different Γ , (a) for elliptical Poiseuille flow at $\psi_x = 0.1$ and $\psi_y = 0.08$, (b) for plane Poiseuille flow at $\psi_x = \psi = 0.1$ and $\psi_y = 0$ and (c) for Hagen-Poiseuille flow at $\psi_x = \psi_y = \psi = 0.1$, plotted on the xz -plane at $\alpha = 0.2$, and $P_0 = 0.1$.

of the particle on the xz - (or yz -) plane in all three Poiseuille flows results from the point force applied at the centre of the particle. The deformed shape of the particle also depends on the material property (Γ , defined following eqn (6)). The shape is plotted on the xz -plane for different Γ for the elliptical Poiseuille [Fig. 6(a)], plane Poiseuille [Fig. 6(b)], and Hagen-Poiseuille [Fig. 6(c)] flows. As is evident from the Fig. 6, the particle exhibits reduced volumetric deformation for larger values of Γ , compared to lower values for all three Poiseuille flows.

3. Deformed shape of the elastic particle and a drop in a plane Poiseuille flow

In the literature, it has been reported that an incompressible simple/active compound spherical drop in a plane Poiseuille flow at the centreline, deforms to a three-lobe shape at $O(Ca)$, [13, 16] due to the hexapolar component of the flow. Here, Ca is the capillary number defined as the ratio of viscous forces to surface tension forces. The three-lobe shape at $O(Ca)$ of the active

compound drop at zero activity is shown in Fig. 7(a).[16] As the activity strength increases, the shape changes from the three-lobe structure. We analyse and compare the leading order shape dynamics of the active compound drop with that of the elastic particle translating in the same flow, with the reference pressure set to zero. At the centreline, the Poiseuille flow reduces to a linear combination of uniform and quadratic flow components. The results presented up to section III D 2 correspond to the particle translating in only the quadratic component of the flow. To the leading order, we can superimpose the deformation of the elastic particle in the quadratic component with that in the uniform component to get the particle's shape for the comparison. The superposition is owing to the linearity of the boundary conditions; $O(1)$ velocity boundary conditions [eqn (30) and (31)] and $O(\alpha)$ stress boundary conditions [eqn (34)-(36)]. We carried out the calculations for the particle translating in the uniform and quadratic components, with the rescaled velocity as V_{max} . The expressions for the surface deformation in both the uniform and quadratic components are given in Appendix D. The elastic particle also deforms to the three-lobe shape, in the flow

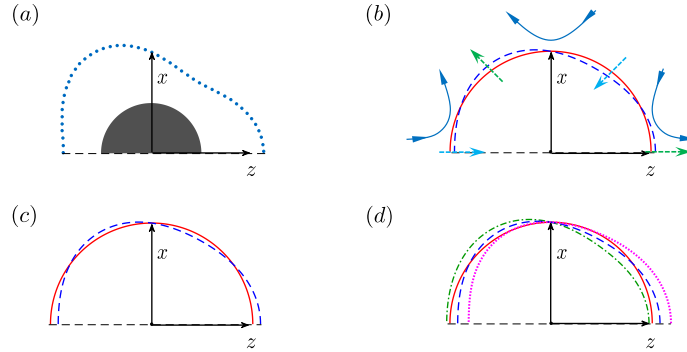


FIG. 7. (a) Deformed shape of the compound drop at zero activity.[16] (b) Deformed shape of the elastic particle as it translates with V_{max} in plane Poiseuille flow, corresponding to (b) γ , and (c) γ and τ . (d) Variation in the deformed shape of the particle for different V_0 relative to V_{max} ; dash-dot for $V_0 = 0.8V_{max}$, dashed for $V_0 = V_{max}$, and dotted for $V_0 = 1.2V_{max}$. Parameters: $\alpha = 0.4$, $\psi = 0.5$, $\Gamma = 2$, and $P_0 = 0$. In (b), the arrows (blue) outside the deformed shape represent γ , and arrows with dotted lines represent the compression (light blue) or extension (green) of the particle depending on the direction of the arrows. The undeformed shape is shown using a red solid line.

field corresponding to γ [Fig. 7(b)] and a nearly three-lobe shape in the complete flow (with additional deformation arising from τ) [Fig. 7(c)]. Further, the particle does not deform in the flow field arising from \mathbf{Q} , same as in the drop at $O(Ca)$. [13, 16] Interestingly, the deformed shape of the elastic particle is also influenced by the velocity of the particle itself. The three-lobe shape

transforms into a distinct shape when the particle translates at a velocity different from the V_{max} , as shown in Fig. 7(d). Such a shape change from the three-lobe shape is also reported for the active compound drop with an increase in activity strength.[16] Therefore, the manipulation of the elastic particle embedded with a magnetic bead using an external magnetic field is analogous to the manipulation of the active compound drop using the strength of the activity. We also note that the reference pressure does not affect the deformed shape of the drop owing to its incompressibility, whereas for the elastic particle considered here, a nonzero reference pressure induces compression in the particle without modifying its leading-order deformed shape.

IV. SUMMARY

We build on the theoretical framework developed in Verma et al.,[7] where the dynamics of an internally actuated elastic particle has been analysed as it translates parallel to a rigid wall in a quiescent fluid. The particle models the response of a spherical polymer bead embedded with a single magnetic particle at its undeformed centre. The external magnetic force/torque acting on such a bead can be effectively modelled as a localised force/torque, using a point force/torque approach, given that the embedded magnetic particle is much smaller in size compared to the bead size. In the present work, the elastic particle is constrained to translate in a general unbounded quadratic flow using a point force/torque approach. We consider that the particle is weakly elastic and compressible in nature. The dynamics and morphology of the particle are analysed in the Stokes limit, neglecting gravitational effects. The fluid and the particle are modelled using the Stokes equations and the Navier elasticity equations, respectively. The results for the particle motion in the general quadratic flow are presented in section III and the results are simplified further for the particle translating with V_{max} along the channel centreline in the quadratic component of: 1) elliptical Poiseuille flow discussed in section III A, 2) plane Poiseuille flow discussed in section III B and 3) Hagen-Poiseuille flow discussed in section III C. The velocity, pressure, displacement, point force, and point torque are obtained until $O(\alpha^2)$. In the general quadratic flow, the effects of elasticity appear as an external force at $O(\alpha)$ and is aligned with the velocity of the particle (z -axis) and the force at $O(\alpha^2)$ has components along all three axes given in eqn (43). In contrast, the external force until $O(\alpha^2)$ is aligned with the particle velocity in all three Poiseuille flows given in eqn (54), (62) and (70). In the general quadratic flow, the external torque due to the elastic effects appears at $O(\alpha)$ and $O(\alpha^2)$ given in eqn (44), while the torque is zero in all three Poiseuille flows. The

streamlines for the quadratic flow and its irreducible components, and those of the total velocity field (ambient plus disturbance fields) are plotted in a laboratory frame for the elliptical Poiseuille [Figs. 2(a)-(h)], plane Poiseuille [Figs. 3(a)-(h)] and Hagen-Poiseuille [Figs. 4(a)-(f)] flows. The γ component of the Poiseuille flows exhibits the extensile-compressive hexapolar structure, which is responsible for generating the three-lobe shape of the deformable particle when subjected to this flow component. The \mathbf{Q} component leads to a deformation of the elastic particle due to the compressibility of the particle. The τ component leads to a deformation of the particle similar to that experienced by the particle in a uniform flow. The final deformed shape of the particle is determined by the force distribution arising from the equilibrium of hydrodynamic forces, the point force, and the point torque. The variation in the shape of the particle is plotted for different confinement ratios (ψ) and material property (Γ), as shown in Figs. 5 and 6, respectively. The deformation exhibited by the particle increases with the increase in ψ or decrease in Γ and vice versa.

We also compare the leading-order deformed shape of the elastic particle at the centreline in a plane Poiseuille flow with that of a drop in the same flow.[16] While the drop exhibits a three-lobe shape in the flow, the elastic particle can also exhibit a similar shape depending on the velocity ratio V_0/V_{max} , as shown in [Fig. 7(d)]. The shape variation of the elastic particle with the velocity ratio is analogous to that of an active compound drop with changing activity strength. The deformed shape will also depend on the force distribution acting on the particle. In a Hagen-Poiseuille flow, an incompressible neo-Hookean sphere subjected to an axial body force and moving along the centerline deforms into a bullet-like shape, an anti-bullet shape, or retains its spherical shape, depending on the magnitude of the external body force and viscous forces.[22] Such a shape will not be observed in the elastic particle considered here because of a change in the force distribution arising from the balance of the point force/torque and the hydrodynamic forces. A thorough understanding of the force distribution acting on a deformable particle is essential for studying the particle dynamics. Our analysis plays a crucial role in understanding the fluid-particle interaction and in determining the steady-state morphology of an elastic particle translating in quadratic flows. The analytical framework developed in this study can be extended to explore the behaviour of viscoelastic/nonlinear elastic polymer beads in quadratic flows.

V. DATA AVAILABILITY

†Electronic supplementary information (ESI): The velocity, pressure fields at $O(1)$ and displacement field at $O(\alpha)$ for the general quadratic flow; simplified results for the quadratic components of the Poiseuille flows.

‡Electronic supplementary information (ESI): The constants needed for the determination of the disturbance velocity and pressure fields at $O(\alpha)$; the displacement field at $O(\alpha^2)$; the disturbance velocity and pressure fields at $O(\alpha^2)$ are available in a Wolfram Mathematica sheet.

Appendix A: Series solutions to the Stokes and continuity equations

The radial (v_r), tangential (v_θ), and azimuthal (v_ϕ) components of the velocity field are given by

$$v_r = \sum_{n=1}^{\infty} \sum_{m=0}^n \left[\left(\frac{\xi^{-n}(n+1)}{2(2n-1)} P_n^m [a[m,n] \cos m\phi + \tilde{a}[m,n] \sin m\phi] \right) - (\xi^{-n-2}(n+1) P_n^m [b[m,n] \cos m\phi + \tilde{b}[m,n] \sin m\phi]) \right], \quad (\text{A1})$$

$$v_\theta = \sum_{n=1}^{\infty} \sum_{m=0}^n \left[\left(\frac{\xi^{-n}(n-2)}{2n(2n-1)(2n+1) \sin \theta} [(n+1)(n+m) P_{n-1}^m - n(n-m+1) P_{n+1}^m] \right) [a[m,n] \cos m\phi + \tilde{a}[m,n] \sin m\phi] - \left(\frac{\xi^{-n-2}}{(2n+1) \sin \theta} [(n+1)(n+m) P_{n-1}^m - n(n-m+1) P_{n+1}^m] \right) \times [b[m,n] \cos m\phi + \tilde{b}[m,n] \sin m\phi] + \left(\frac{\xi^{-n-1} m}{\sin \theta} P_n^m [-v[m,n] \sin m\phi + \tilde{v}[m,n] \cos m\phi] \right) \right] \quad (\text{A2})$$

and

$$\begin{aligned}
v_\phi = & \sum_{n=1}^{\infty} \sum_{m=0}^n \left[\left(-\frac{\xi^{-n}(n-2)m}{2n(2n-1)\sin\theta} P_n^m [-a[m,n]\sin m\phi \right. \right. \\
& \left. \left. + \tilde{a}[m,n]\cos m\phi \right) \right. \\
& + \left(\frac{\xi^{-n-2}m}{\sin\theta} P_n^m [-b[m,n]\sin m\phi + \tilde{b}[m,n]\cos m\phi] \right) \\
& + \left(\frac{\xi^{-n-1}}{(2n+1)\sin\theta} [(n+1)(n+m)P_{n-1}^m - n(n-m+1)P_{n+1}^m] \right) \\
& \left. \times (v[m,n]\cos m\phi + \tilde{v}[m,n]\sin m\phi) \right], \tag{A3}
\end{aligned}$$

respectively. The pressure field is given by

$$p = \sum_{n=1}^{\infty} \sum_{m=0}^n [\xi^{-n-1} P_n^m (a[m,n]\cos m\phi + \tilde{a}[m,n]\sin m\phi)]. \tag{A4}$$

Above, P_n^m denotes $P_n^m(\cos\theta)$, the associated Legendre polynomial of order m and degree n . The constants, $a[m,n]$, $\tilde{a}[m,n]$, $b[m,n]$, $\tilde{b}[m,n]$, $v[m,n]$, and $\tilde{v}[m,n]$ are determined from the no-slip and no-penetration boundary conditions at the surface of the particle.

Appendix B: Series solutions to the Navier elasticity equations

The radial (u_r), tangential (u_θ), and azimuthal (u_ϕ) components of the displacement field are given by

$$\begin{aligned}
u_r = & \frac{1}{4\pi\xi} \left[F_z \cos\theta + F_x \cos\phi \sin\theta + F_y \sin\theta \sin\phi \right] \\
& + \sum_{n=0}^{\infty} \sum_{m=0}^n [\xi^{n+1} P_n^m (b1[m,n]\cos m\phi + b0[m,n]\sin m\phi)] \\
& + \sum_{n=1}^{\infty} \sum_{m=0}^n [\xi^{n-1} P_n^m (c1[m,n]\cos m\phi + c0[m,n]\sin m\phi)], \tag{B1}
\end{aligned}$$

$$\begin{aligned}
u_\theta = & \frac{(3+\Gamma)}{8\pi(2+\Gamma)\xi} \left(-F_z \sin \theta + \cos \theta [F_x \cos \phi + F_y \sin \phi] \right) \\
& + \frac{1}{8\pi\xi^2} \left(T_y \cos \phi - T_x \sin \phi \right) + \frac{1}{\sin \theta} \left[\sum_{n=1}^{\infty} \sum_{m=0}^n \left(\frac{\xi^n m(2n+1)}{n(n+1)} \right. \right. \\
& \left. \left. \times P_n^m [-a1[m,n] \sin m\phi + a0[m,n] \cos m\phi] \right) \right] \\
& + \frac{1}{\sin \theta} \left[\sum_{n=1}^{\infty} \sum_{m=0}^n \left(\frac{\xi^{n+1} [\Gamma(n+3) + (n+5)]}{(2n+1)(n+1)[\Gamma n + (n-2)]} \right. \right. \\
& \left. \left. \times [n(n-m+1)P_{n+1}^m - (n+1)(n+m)P_{n-1}^m] \right) \right] \\
& \left. \times (b1[m,n] \cos m\phi + b0[m,n] \sin m\phi) \right] \\
& + \frac{1}{\sin \theta} \left[\sum_{n=1}^{\infty} \sum_{m=0}^n \left(\frac{\xi^{n-1}}{(2n+1)n} [n(n-m+1)P_{n+1}^m - (n+1) \right. \right. \\
& \left. \left. \times (n+m)P_{n-1}^m] \right) (c1[m,n] \cos m\phi + c0[m,n] \sin m\phi) \right] \tag{B2}
\end{aligned}$$

and

$$\begin{aligned}
u_\phi = & \frac{(3+\Gamma)}{8\pi(2+\Gamma)\xi} \left(F_y \cos \phi - F_x \sin \phi \right) \\
& + \frac{1}{8\pi\xi^2} \left(T_z \sin \theta - \cos \theta [T_x \cos \phi + T_y \sin \phi] \right) \\
& + \frac{1}{\sin \theta} \left[\sum_{n=0}^{\infty} \sum_{m=0}^n \left(\frac{-\xi^n}{(n+1)} (n-m+1) P_{n+1}^m \right. \right. \\
& \left. \left. \times [a1[m,n] \cos m\phi + a0[m,n] \sin m\phi] \right) + \sum_{n=1}^{\infty} \sum_{m=0}^n \left(\frac{\xi^n}{n} (n+m) \right. \right. \\
& \left. \left. \times P_{n-1}^m [a1[m,n] \cos m\phi + a0[m,n] \sin m\phi] \right) \right] \\
& + \frac{1}{\sin \theta} \left[\sum_{n=0}^{\infty} \sum_{m=0}^n \left(\frac{\xi^{n+1} m [\Gamma(n+3) + (n+5)]}{(n+1)[\Gamma n + (n-2)]} P_n^m \right. \right. \\
& \left. \left. \times [-b1[m,n] \sin m\phi + b0[m,n] \cos m\phi] \right) \right] + \frac{1}{\sin \theta} \left[\sum_{n=1}^{\infty} \sum_{m=0}^n \right. \\
& \left. \left(\frac{\xi^{n-1} m}{n} P_n^m [-c1[m,n] \sin m\phi + c0[m,n] \cos m\phi] \right) \right], \tag{B3}
\end{aligned}$$

respectively. Here, the constants, $a1[m,n]$, $a0[m,n]$, $b1[m,n]$, $b0[m,n]$, $c1[m,n]$, and $c0[m,n]$ are determined from the stress continuity at the particle surface.

Appendix C: Formulation of point force/torque in the presence of body force

Consider that the nondimensional body force term, $\mathbf{K}_p = \rho_p \mathbf{g} R_0 / G$, where ρ_p and \mathbf{g} are the particle density and gravity, respectively, is also included in the Navier elasticity equations. The volume integral of the equation yields

$$\int_{\text{Vol}_1} (\nabla \cdot \hat{\boldsymbol{\sigma}}) dV = - \left(\mathbf{F} + \int_{\text{Vol}_1} \mathbf{K}_p dV \right). \quad (\text{C1})$$

Here, Vol_1 is the volume of the deformed sphere of area Area_1 , as shown in Fig. 8. The term on the

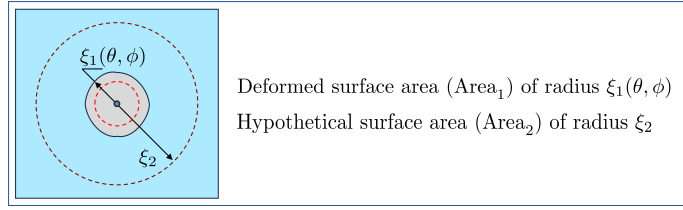


FIG. 8. Schematic of the deformed sphere, showing different regions of interest. Volume of deformed sphere (Vol_1) of radius $\xi_1(\theta, \phi)$ and outside the deformed sphere (Vol_2) between radial distance $\xi_1(\theta, \phi)$ and ξ_2 .

left-hand side of eqn (C1) can be converted to an area integral using Gauss's divergence theorem. The resulting equation after applying the stress continuity at the deformed interface is obtained as

$$\alpha \int_{\text{Area}_1} (\boldsymbol{\sigma} \cdot \hat{\mathbf{n}}) dA = - \left(\mathbf{F} + \int_{\text{Vol}_1} \mathbf{K}_p \xi^2 \sin \theta d\xi d\theta d\phi \right). \quad (\text{C2})$$

Here, Area_1 itself is a part of the solution. The fluid stress distribution over Area_1 can be expressed in terms of the body force within volume Vol_2 enclosed between Area_1 and a hypothetical surface area (Area_2) outside the deformed surface. Accordingly, eqn (C2) can be written as

$$\alpha \int_{\text{Area}_2} (\boldsymbol{\sigma} \cdot \hat{\mathbf{n}}_2) dA = - \left(\mathbf{F} + \int_{\text{Vol}_1} \mathbf{K}_p \xi^2 \sin \theta d\xi d\theta d\phi + \int_{\text{Vol}_2} \mathbf{K}_f \xi^2 \sin \theta d\xi d\theta d\phi \right). \quad (\text{C3})$$

Here, $\hat{\mathbf{n}}_2$ is the unit outward normal vector to the Area_2 and $\mathbf{K}_f = \rho_f R_0^2 \mathbf{g} / (\mu V_0)$. To simplify the calculation, Area_2 is considered as the surface area of a sphere. Note that the point force at the leading-order induces the stress inside the particle at $O(\alpha)$, and the point force at $O(\alpha)$ induces stress at $O(\alpha^2)$. As is evident from eqn (C3), in the absence of body force ($\mathbf{K}_p = \mathbf{K}_f = 0$), as in the presented work, the integral of the $\boldsymbol{\sigma} \cdot \hat{\mathbf{n}}_2$ over Area_2 give the external point force directly.

Similarly, one can also obtain the expression for point torque. The resulting expression is obtained as

$$\alpha \int_{\text{Area}_2} (\mathbf{x} \times [\boldsymbol{\sigma} \cdot \hat{\mathbf{n}}_2]) dA = - \left(\mathbf{T} + \int_{\text{Vol}_1} [\mathbf{x} \times \mathbf{K}_p] \xi^2 \sin \theta d\xi d\theta d\phi + \alpha \int_{\text{Vol}_2} [\mathbf{x} \times \mathbf{K}_f] \xi^2 \sin \theta d\xi d\theta d\phi \right). \quad (\text{C4})$$

Here, \mathbf{x} is the non-dimensional position vector measured from the centre of the undeformed particle and $\xi = |\mathbf{x}|$. In the absence of body force ($\mathbf{K}_p = \mathbf{K}_f = 0$), the external point torque can be determined directly from the fluid stress distribution using eqn (C4).

Appendix D: Surface deformation ($f^{(1)}$) in uniform and quadratic component of plane Poiseuille flow

The velocity of the particle ($V_0 \hat{\mathbf{k}}$) along the centreline in the plane Poiseuille flow is decomposed into the velocity in the uniform flow component, $V_{0,un} \hat{\mathbf{k}}$, and the velocity in the quadratic flow component, $V_{0,q} \hat{\mathbf{k}}$, such that $V_0 = V_{0,un} + V_{0,q}$. The flow velocity inside the channel is maximum at the centreline (V_{max}), and is chosen as the velocity scale for the analysis below. The surface deformation of the particle at the leading-order in a uniform component of magnitude V_{max} is represented as $f_{uni,p}^{(1)}$ and is obtained as

$$f_{uni,p}^{(1)} = \frac{3(V_{r,un} - 1)(5 + 2\Gamma[4 + \Gamma]) \cos \theta}{2(2 + \Gamma)(2 + 3\Gamma)}. \quad (\text{D1})$$

Above, $V_{r,un}$ is the ratio of particle velocity in the uniform component to the maximum Poiseuille flow velocity; $V_{r,un} = V_{0,un}/V_{max}$. The surface deformation of the particle in the quadratic component is denoted by $f_{qad,p}^{(1)}$ and is obtained as

$$f_{qad,p}^{(1)} = \frac{1}{64(2 + \Gamma)(2 + 3\Gamma)} \left[-64P_0(2 + \Gamma) + \cos \theta (96V_{r,q}(5 + 2\Gamma(4 + \Gamma)) + (260 + (136 - 21\Gamma)\Gamma)\psi^2 + 35(2 + \Gamma)(2 + 3\Gamma)\psi^2(\cos 2\theta - 2 \cos 2\phi \sin^2 \theta)) \right]. \quad (\text{D2})$$

Above, $V_{r,q} = V_{0,q}/V_{max}$. The surface deformation given in eqn (D2) simplifies to that given in eqn (60) by substituting $V_{r,q} = 1$ in eqn (D2), which corresponds to the case of the particle translating

at V_{max} along the centreline in the quadratic component of the plane Poiseuille flow.

- [1] Philippova, O, Barabanova, A, Molchanov, V & Khokhlov, A 2011 Magnetic polymer beads: Recent trends and developments in synthetic design and applications. *European Polymer Journal* **47**(4), 542–559.
- [2] Seyfoori, A, Seyyed Ebrahimi, SA, Samandari, M, Samiei, E, Stefanek, E, Garnis, C & Akbari, M 2023 Microfluidic-Assisted CTC Isolation and In Situ Monitoring Using Smart Magnetic Microgels. *Small* **19**(16), 2205320.
- [3] Sung, B, Kim, M-H & Abelman, L 2021 Magnetic microgels and nanogels: Physical mechanisms and biomedical applications. *Bioengineering & Translational Medicine* **6**(1), e10190.
- [4] Safarik, I, Safarikova, M & Forsythe, SJ 1995 The application of magnetic separations in applied microbiology.
- [5] Safarikova, M & Safarik, I 2001 The application of magnetic techniques in biosciences. *Physical Separation in Science and Engineering* **10**(4), 223–252.
- [6] Moerland, CP, Van IJzendoorn, LJ & Prins, MWJ 2019 Rotating magnetic particles for lab-on-chip applications—a comprehensive review. *Lab on a Chip* **19**(6), 919–933.
- [7] Verma, S, Dinesh, B & Marath, NK 2025 Dynamics of an internally actuated weakly elastic sphere translating parallel to a rigid wall. *Journal of Fluid Mechanics* **1021**, A50.
- [8] Cavett, V, Chan, AI, Cunningham, CN & Paegel, BM 2023 Hydrogel-encapsulated beads enable proximity-driven encoded library synthesis and screening. *ACS Central Science* **9**(8), 1603–1610.
- [9] Tobias, C, López-Puertollano, D, Abad-Somovilla, A, Mercader, JV, Abad-Fuentes, A & Rurack, K 2024 Development of Simple and Rapid Bead-Based Cytometric Immunoassays Using Superparamagnetic Hybrid Core–Shell Microparticles. *ACS Measurement Science Au* **4**(6), 678–688.
- [10] Wang, S, Tai, C-W & Narsimhan, V 2020 Dynamics of spheroids in an unbound quadratic flow of a general second-order fluid. *Physics of Fluids* **32**(11).
- [11] Tai, C-W, Wang, S & Narsimhan, V 2020 Cross-stream migration of non-spherical particles in a second-order fluid—theories of particle dynamics in arbitrary quadratic flows. *Journal of Fluid Mechanics* **895**, A6.
- [12] Yang, S-M & Lee, T-Y 1989 Motions of a fluid drop in linear and quadratic flows. *Korean Journal of Chemical Engineering* **6**, 321–329.

- [13] Nadim, A & Stone, H A 1991 The motion of small particles and droplets in quadratic flows. *Studies in Applied Mathematics* **85**, 53–73.
- [14] Favelukis, M 2022 A drop in a nonlinear shear flow. *Journal of Fluid Mechanics* **941**, A50.
- [15] Haber, S & Hetsroni, G 1971 The dynamics of a deformable drop suspended in an unbounded Stokes flow. *Journal of Fluid Mechanics* **49**, 257–277.
- [16] Chaithanya, K V S, Singeetham, P K & Thampi, S P 2023 Active compound particles in a quadratic flow: hydrodynamics and morphology. *Soft Matter* **19**, 7963–7978.
- [17] Razzaghi, A & Ramachandran, A 2023 Deformation of a Hele–Shaw drop undergoing quadratic flow. *Physics of Fluids* **35**.
- [18] Hou, H W, Li, Q S, Lee, G Y H, Kumar, A P, Ong, C N & Lim, C T 2009 Deformability study of breast cancer cells using microfluidics. *Biomedical Microdevices* **11**, 557–564.
- [19] Villone, M M & Maffettone, P L 2019 Dynamics, rheology, and applications of elastic deformable particle suspensions: a review. *Rheologica Acta* **58**, 109–130.
- [20] Zhang, H, Kay, A, Forsyth, N R, Liu, K-K & El Haj, A J 2012 Gene expression of single human mesenchymal stem cell in response to fluid shear. *Journal of Tissue Engineering* **3**, 2041731412451988.
- [21] Jin, J, Jaspers, R T, Wu, G, Korfage, J A M, Klein-Nulend, J & Bakker, A D 2020 Shear stress modulates osteoblast cell and nucleus morphology and volume. *International Journal of Molecular Sciences* **21**, 8361.
- [22] Finney, S M, Hennessy, M G, Münch, A & Waters, S L 2024 The impact of confinement on the deformation of an elastic particle under axisymmetric tube flow. *IMA Journal of Applied Mathematics* **89**, 498–532.
- [23] Anselmo, A C & Mitragotri, S 2017 Impact of particle elasticity on particle-based drug delivery systems. *Advanced Drug Delivery Reviews* **108**, 51–67.
- [24] Tam, C K W & Hyman, W A 1973 Transverse motion of an elastic sphere in a shear field. *Journal of Fluid Mechanics* **59**, 177–185.
- [25] Murata, T 1980 On the deformation of an elastic particle falling in a viscous fluid. *Journal of the Physical Society of Japan* **48**, 1738–1745.
- [26] Murata, T 1981 Deformation of an elastic particle suspended in an arbitrary flow field. *Journal of the Physical Society of Japan* **50**, 1009–1016.
- [27] Peng, S, Zhang, M, Niu, X, Wen, W, Sheng, P, Liu, Z & Shi, J 2008 Magnetically responsive elastic microspheres. *Applied Physics Letters* **92**.

- [28] Nasouri, B, Khot, A & Elfring, G J 2017 Elastic two-sphere swimmer in Stokes flow. *Physical Review Fluids* **2**, 043101.
- [29] Johns, L E & Narayanan, R 2002 *Interfacial Instability*. Springer Science & Business Media.
- [30] Leal, L G 2007 *Advanced Transport Phenomena: Fluid Mechanics and Convective Transport Processes*. Cambridge University Press.
- [31] Coope, J A R, Snider, R F & McCourt, F R 1965 Irreducible cartesian tensors. *The Journal of Chemical Physics* **43**, 2269–2275.